Characterisation of subsurface oxidation damage in Ni based superalloy, RR1000

Cruchley, S.; Taylor, Mary; Evans, H. E.; Hardy, M. C.; Child, D. J.

DOI:
10.1179/1743284714Y.0000000541

This is the Author's copy of an Accepted Manuscript of an article published by Taylor & Francis in Materials Science and Technology on 14th April 2014, available online:
http://www.tandfonline.com/doi/abs/10.1179/1743284714Y.0000000541

CHARACTERISATION OF THE SUB-SURFACE OXIDATION DAMAGE IN THE NI-BASED SUPERALLOY, RR1000

S. Cruchley[1], M.P. Taylor[1], H. E. Evans[1], M.C. Hardy[2] and D.J. Child[2]

[1]School of Metallurgy and Materials, University of Birmingham, Birmingham, B15 2TT, UK
[2]Rolls-Royce plc, Derby, DE24 8BJ, UK

Key words: Oxidation, Internal Oxide, Al_2O_3, Ni-based superalloy.

ABSTRACT

Isothermal oxidation of the Ni-based superalloy, RR1000, has been performed at 700, 750 and 800ºC for exposure periods up to 2000 hours. A chromia external oxide scale with an outer layer of rutile was formed together with extensive internal oxidation of aluminium, both intragranularly and intergranularly. The internal oxidation was associated with a deeper γ′ particle free zone. Extensive metallographic measurements of both the depth of internal oxidation and of the γ′ particle free zone were made. The kinetics in each case approximated well to parabolic. Possible rate controlling processes are discussed.

INTRODUCTION

The high temperatures and stresses experienced in high pressure turbine disc rotors necessitate the use of Ni-based superalloys as the material of choice. These alloys have been optimised microstructurally and compositionally for use in these highly demanding conditions. In order to improve engine efficiency and reduce CO_2 emissions the engine operating temperatures are being regularly increased. High temperature degradation through oxidation is now extremely important since it has the potential to reduce component lives. Most of the current disc alloys in use are characteristic of chromia-forming Ni-based superalloys in that they have a sufficient chromium content to form an initial chromia layer, but they also suffer from extensive internal oxidation, particularly of aluminium.[1-10]

The formation of internal oxides is undesirable since they can have a significant detrimental effect on the mechanical properties of the alloy. This is especially the case if the internal oxide causes strengthening elements to be removed from the alloy.[11] This can, in some cases, be accompanied by a grain recrystallised zone around and underneath these internal oxides.[8] Internal oxides that form at alloy grain boundaries often have an acicular morphology and it is possible for these to act as preferential crack initiation sites. Additionally, the volume expansion that occurs on formation of the internal oxides can lead to compressive stresses that appear to be relaxed by the formation of metallic protrusions within the oxide scale as a result of outward alloy creep. This has been seen in a number of different alloy systems.[12-17]

The development of internal oxidation has been extensively investigated in many systems and has been well reviewed in Ni-based alloys.[11, 18] A common finding is that the deepest internal oxides form intergranularly, as reported in Ni-Al[19, 20] and Ni-Cr alloys.[12, 21, 22] The diffusion of oxygen within the internally oxidised region has also been investigated in these simple alloys.[23, 24] The purpose of the present study was to examine, in detail, the sub-surface oxidation damage caused by long term high temperature exposure of the Ni-based superalloy, RR1000, and to establish the kinetics of this form of degradation.

EXPERIMENTAL PROCEDURE

An advanced Ni-based superalloy, RR1000, was produced using a powder metallurgy route followed by a heat treatment to obtain a uniform distribution of secondary and tertiary γ′ (nominally, $Ni_3(Al,Ti)$) particles along with a coarse grain size of between 30 to 50 μm. The nominal composition of the alloy is contained in Table 1.

Isothermal oxidation testing was conducted over a temperature range of 700°C-800°C in laboratory air for prolonged periods of time (up to 2000 hours). The specimens were cut to size (20 mm x 10 mm x 2-3 mm) using a precision cutting machine. All the surfaces were ground and polished to produce a surface finish, R_a, of approximately 0.3 μm and to remove the damage caused by the cutting process. All edges and corners were chamfered to reduce stress concentrators and polished to the same surface finish. Batches of specimens were placed into open alumina boats then inserted into single zone tube furnaces. The furnaces were calibrated to ±1°C using an N-type thermocouple and, at selected time intervals, a specimen was removed from the batch for examination before the high temperature exposure continued for the remainder of the batch.

The specimens were prepared for cross-sectional analysis following oxidation testing by sputtering with gold followed by nickel-plating and vacuum impregnation in a low viscosity and low shrinkage resin. The cross sections were ground on wet SiC papers down to 2500 grit followed by polishing

using progressively finer diamond solutions to a final stage of 0.25 μm. The sections were chemical etched using a selective γ′ etch described by Huang et al.[25]

Cross-sectional analysis was performed using a field emission gun Jeol 7000F scanning electron microscope (SEM) capable of undertaking energy dispersion spectroscopy (EDS) and wavelength dispersion spectroscopy (WDS). Image analysis was performed on backscattered electron images (BSE) using Image J 1.45 analysis software. The depths of the internal oxide (both intergranular and intragranular) were measured, as shown in Fig. 1, together with the depths of the γ′ particle free zones. 50 measurements were taken from 10 images for intragranular depth measurements but only 10 measurements were performed for the intergranular penetrations due to their infrequent occurrence.

RESULTS AND DISCUSSION

Oxide characterisation

Complex sub-surface damage resulting from the prolonged high temperature exposures occurred underneath a dense external oxide scale. The typical morphology of the oxides can be seen in Fig. 1 and shows the presence of both intergranular and intragranular oxides beneath the surface oxide scale. The intergranular penetrations form continuous oxides down the grain boundaries whereas intragranular oxides occur as discrete precipitates within the grains. This kind of intergranular oxide morphology has been found previously in similar Ni-based superalloys[1, 8] as well as in this current alloy.[4, 5] These internal oxides are predominantly alumina. The development of the internal oxides over time can be seen in Fig. 2. The deeper alumina penetrations at the grain boundaries suggest that these sites act as short circuit diffusion pathways.[26]

The etched microstructure of Fig. 3 also shows how the region of internal oxidation is depleted of γ′ precipitates and that this particle free zone (PFZ) extends ahead of the internal oxidation front. No recrystallisation of the grains was found in this alloy within the depletion zone although recrystallisation has been found in both Ni-based superalloys, ME3 and RR1000 (with a fine grained microstructure [4-6 μm]).[3, 8] TiN particles were also present within the γ′particle free zone but were only seen at 800°C at long exposure times (2000 hours). As has been found in several other alloying systems and in a previous study on this alloy[4], metallic protrusions or metallic nodules were present in the external oxide scale (fig. 3). It is likely that these have been formed by outward alloy creep from the weak γ′particle free zone to accommodate the increase in volume resulting from internal oxide formation.[12-17] No Cr-rich phases were found in the vicinity of the oxidation zone, presumably because of the depletion of Cr to the oxide layer. Remote form the oxidation front, grain boundary phases, containing Cr and Mo were present.[27] These presumably were $M_{23}C_6$-type carbides although later transformations to σ-phase compositions may occur.[28]

Kinetics of Internal Oxidation (IOZ) and Particle Free (PFZ) Zones

Extensive measurements of the thicknesses of the internal oxidation zone (IOZ) and γ′ particle free zone (PFZ) at multiple temperatures and time periods have been performed, as described earlier. These measurements were normally distributed and typical results are shown in Table 2 for exposures at 2000 hours at the three test temperatures. The internal oxide penetration depth, ℓ, with time at each of the temperatures is shown in Fig. 4 for intergranular (ℓ_{gb}) and intragranular (ℓ_{tr}) locations, together with the best-fit parabolic curve. In all cases, the kinetics are approximated, reasonably, by parabolic behaviour:

$$\lambda_{gb} = \left(\left(k_{p\lambda}\right)_{gb}.t\right)^{0.5} \quad (1)$$

$$\lambda_{tr} = \left(\left(k_{p\lambda}\right)_{tr}.t\right)^{0.5} \quad (2)$$

where t is exposure time (seconds) and $k_{p\ell}$ is the appropriate parabolic rate constant ($m^2.s^{-1}$). The best-fit parabolic rate constants for IOZ penetration are shown in Table 3.

The corresponding curves for the depth, y, of the γ′ PFZ are shown in Fig. 5. Again, parabolic kinetics are reasonably obtained and the appropriate rate constants for intergranular, $(k_{py})_{gb}$, and intragranular, $(k_{py})_{tr}$, behaviour are also given in Table 3. As expected, these are larger than the corresponding rate constants for internal oxidation. Using the square root of the ratio of rate constants in Table 3 indicates that the intragranular PFZ is approximately 6% deeper than the IOZ at 700°C and approximately 31% deeper at 800°C; the corresponding values for intergranular penetration are approximately 23% and 27% at 700 and 800°C, respectively.

The temperature dependence of the respective rate constants for internal oxide formation are shown in the Arrhenius plot of Fig. 6. The present results are obviously limited (three temperatures only) and do not lie on a particularly convincing line (although the $R^2 = 0.94$ for intergranular and 0.89 for intragranular). Nevertheless, they fall within the overall trend displayed by other similar alloys as can be seen from the figure. The values of activation energies obtained from the slopes of the broken lines shown are given in Table 4 and are essentially identical at 295 $kJ.mol^{-1}$. The best-fit rate equations for each morphology are given below as Equations (3) and (4).

Intragranular penetrations

$$\left(k_{p\lambda}\right)_{tr} = 3.75x10^{-3}\exp^{\left[-\frac{297426}{8.314T}\right]} \quad m^2.s^{-1} \quad (3)$$

Intergranular penetrations

$$\left(k_{p\lambda}\right)_{gb} = 5.74x10^{-3}\exp^{\left[-\frac{292718}{8.314T}\right]} \quad \mathrm{m}^2.\mathrm{s}^{-1} \tag{4}$$

The temperature dependence of the growth of the PFZ was similarly obtained from an Arrhenius plot to obtain the values of "activation energy" also shown in Table 4. These are a little higher than those found for the growth of the IOZ but reflect a combination of the temperature dependences of the IOZ growth, of aluminium diffusion into the IOZ and also the local aluminium concentration for γ′ solution. It is a complex situation that cannot be defined by a singly-activated process. Nevertheless, the "activation energy" provides a very useful means of predicting the temperature dependence of PFZ growth, as given in Equation (5) and (6).

PFZ associated with intragranular penetrations

$$\left(k_{py}\right)_{tr} = 4.98x10^{-1}\exp^{\left[-\frac{335792}{8.314T}\right]} \quad \mathrm{m}^2.\mathrm{s}^{-1} \tag{5}$$

PFZ associated with intergranular penetrations

$$\left(k_{py}\right)_{gb} = 2.75x10^{-2}\exp^{\left[-\frac{302085}{8.314T}\right]} \quad \mathrm{m}^2.\mathrm{s}^{-1} \tag{6}$$

Possible Rate Controlling Processes

Internal oxidation of alloys is usually considered to be controlled by the rate of diffusion of oxygen within the alloy. This is likely to be the case in the absence of a surface oxide layer, as considered initially by Wagner.[29] In the presence of a protective surface layer, the diffusion model becomes more difficult but Maak[30] has provided a solution for the case where the surface oxide thickens parabolically. Direct application of this model to the present tests cannot be undertaken reliably, however, because the surface oxide thickens with sub-parabolic kinetics and the model requires the measurements to be taken from the original surface. Estimating the position of the original surface is difficult in this alloy due to the formation of metallic protrusions into the surface oxide. Maak's treatment again envisages diffusion within the alloy to be rate determining whereas, in principle, the rate of internal oxidation could be determined by the rate of transport through the surface layer. This becomes more likely when the surface oxide is protective as in the present case. It is also clear that a depletion profile of aluminium develops ahead of the region of internal oxidation as evidenced by a γ′ particle-free zone (PFZ), as shown in Figures 3 and 7. The EDS scan of Fig. 7 demonstrates that the aluminium concentration within the alloy falls rapidly from the bulk value (horizontal line) as the PFZ boundary is crossed and before the IOZ is reached. Since the formation of a particle of new oxide within the alloy requires that the solubility product of alumina is exceeded, it is possible, in principle,

for the supply of aluminium, rather than oxygen, to control the rate of thickening of the internal oxidation zone.

The activation energies for the thickening of the IOZ in the present tests are essentially the same at ~295 kJ.mol^{-1} (Table 4) for both intergranular and intragranular penetration. This is a surprising result since it would be expected that the faster rate of penetration down alloy grain boundaries would have been associated with a lower activation energy commensurate with a fast diffusion path if oxygen transport within the alloy were rate controlling. It needs to be emphasised, however, that these values are based on measurements obtained at only three temperatures and a more comprehensive data set is required. This experimental work is underway.

Conclusions

- Significant sub-surface damage occurs in this alloy from long term, high temperature exposure in an oxidising environment. This consists of an internal oxidation zone with both intragranular and intergranular oxide formation and a γ′particle free zone characterised by elemental depletion of Al.
- The growth rates of internal attack followed a near parabolic rate law. Equations to describe the development of the two zones have been produced.
- The process controlling the development of the sub-surface damage is unclear but it is likely to be a combination of: oxygen transport through the surface oxide, oxygen transport into the alloy and aluminium diffusion to the reaction front.

Acknowledgements

The authors acknowledge, with thanks, the support provided by the Engineering and Physical Sciences Research Council (EPSRC) for financial support and Rolls-Royce plc. for further financial support and the provision of samples.

References

1. J. Chen, P. Rogers and J. Little: *Ox of Met*, 1997, 47, 381-410.
2. D. Kim, C. Jang and W. Ryu: *Ox of Met*, 2009, 71, 271-293.
3. A. Encinas-Oropesa, N.J. Simms, J.R. Nicholls, G.L. Drew, J. Leggett and M.C. Hardy: *Mater High Temp*, 2009, 26, 241-249.
4. M.P. Taylor, H.E. Evans, S. Stekovic and M.C. Hardy: *Mater High Temp*, 2012, 29, 145-150.
5. S. Cruchley, M.P. Taylor, H.E. Evans, P. Bowen, S. Stekovic, M.C. Hardy: Superalloys 2012: 12th International Symposium on Superalloys, TMS, Seven Springs, PA, 2012, 751-758.
6. G.A. Greene and C.C Finfrock: *Ox of Met*, 2001, 55, 505-521.
7. L. Zheng, M. Zhang and J. Dong: *Appl Surf Sci*, 2010, 256, 7510-7515.

8. C.K Sudbrack, S.L. Draper, T.T Gorman, J Telesman, T.P. Gabb and D.R. Hull: Superalloys 2012: 12th International Symposium on Superalloys, TMS, Seven Springs, PA, 2012, 863-872.
9. K.A. Al-Hatab, M.A. Al-Bukhaiti, U. Krupp and M. Kantehm: *Ox of Met*, 2011, 75, 209-228.
10. H. Buscail, S. Perrier and C. Josse: *Materials and Corrosion*, 2011, 62, 416-422.
11. F.H. Stott and G.C. Wood: *Mat Sci Tech*, 1988, 4, 1072-1078.
12. H. Ackermann, G. Teneva-Kosseva, K. Lucka, H. Koehne, S. Richter and J. Mayer: *Corr Sci*, 2007, 49, 3866-3879.
13. J. Issartel, S. Martoia, F. Charlot, V. Parry, R. Estevez and Y. Wouters: *Corr Sci*, 2012, 59, 148-156.
14. P. Huszkowski, S. Ertl, J. Piron-Abellan, N. Christiansen, T. Fler, V. Shemet, L. Singheiser and W. J. Quadakkers: *Mater High Temp*, 2005, 22, 253-262.
15. D. Young: *Mater Sci Forum*, 2011, 969, 1-11.
16. I.M. Edmonds, H.E. Evans and C.N. Jones: *Ox of Met*, 2012, 73, 193-206.
17. J. Issartel, R. Estevez, G. Parry, V. Parry, S. Martoia and Y. Wouters: *Ox of Met*, 2013, 79, 65-72.
18. R.A. Rapp: *Corrosion*, 1965, 21, 382-401.
19. Y. Shida, F.H. Stott, B.D. Bastow, D.P. Whittle and G.C. Wood: *Ox of Met*, 1982, 18, 93-133.
20. F.H. Stott, Y. Shida, D.P. Whittle, G.C. Wood and B.D. Bastow: *Ox of Met*, 1982, 18, 127-146.
21. G.C. Wood, F.H. Stott, D.P. Whittle, Y. Shida and B.D Bastow: *Corr Sci*, 1983, 23, 9-25.
22. C.S Giggins and F.S. Pettit: *Journal of the Electrochemical Society*, 1971, 118, 1782-1790.
23. F.H. Stott, G.C. Wood, D.P. Whittle, B.D. Bastow, Y. Shida and A. Martinez-Villafane: *Solid State Ionics*, 1984, 12, 365-374.
24. A. Martinez-Villafane, F.H. Stott, J.G. Chacon-Nava and G.C. Wood: *Ox of Met*, 2002, 57, 267-279.
25. Z.W. Huang, H.Y. Li, M. Preuss, M. Karadge, P. Bowen, S. Bray and G. Baxter: *Metall Mat Trans A*, 2007, 38A, 1608-1620.
26. D.L. Douglass: *Ox of Met*, 1995, 44, 81-111.
27. S. Cruchley, M.P. Taylor, H.Y. Li, H.E. Evans, P. Bowen, D.J. Child and M.C. Hardy, Proc. 9th Int. Conf. on *Microscopy of Oxidation*, Nottingham, UK, 2014. Accepted in press.
28. R.J. Mitchell, C.M.F. Rae and S. Tin. *Mater. Sci. Technol*, 2005, 21, 125-132
29. C. Wagner: *Z. Elektrochem.*, 1959, 63, 773.
30. F. Maak: *Z. Metallkunde*, 1961, 52, 545-546.

Figure captions:

Figure 1: BSE image showing the oxide morphology of coarse-grained RR1000 oxidised at 800°C for 2000 hours, illustrating how the internal oxide depth measurements were recorded.

Figure 2: BSE images showing the evolution of the internal oxide penetrations over time when oxidised at 800°C.

Figure 3: BSE image showing the sub-surface damage at 800°C for 2000 hours, clearly illustrating a significant γ′ particle free zone. The sample was etched using a chemical etched described by Huang et al.[25]

Figure 4: Plot of intergranular and intragranular internal oxide penetrations against time at a) 700°C, b) 750°C and c) 800°C, with a fit line plotted for each condition according to $\lambda = \left(k_{p\lambda}.t\right)^{0.5}$.

Figure 5: Plot of intergranular and intragranular γ′ particle free zone depth against time at a) 700°C, b) 750°C and c) 800°C, with a fit line plotted for each condition according to $y = \left(k_{py}.t\right)^{0.5}$.

Figure 6: Arrhenius plot of both the intergranular and intragranular internal oxide penetrations along with measurements of several other similar Ni-based superalloys for comparison. Some of the values were recorded from single measurements taken from the literature and so are recorded as instantaneous parabolic rate constants (*).

Figure 7: EDS analysis showing the diffusion profile of the aluminium concentration at 4 μm increments of a specimen oxidised at 800°C for 2000 hours. The dashed line on the micrograph indicates the limits of the γ′ particle free zone. The boundaries of the various zones and the baseline level of aluminium in the alloy are indicated on the profile. Oxygen was not detected in this profile.

Table captions:

Table 1: Nominal composition of RR1000 in atomic and weight %.

Table 2: Sub-surface damage measurements for both intragranular and intergranular internally oxidised internal oxide penetrations and γ′ particle free zone, with one standard deviation.

Table 3: Parabolic rate constants for both intragranular and intergranular internal oxide penetration and intragranular and intergranular γ′ particle free zones.

Table 4: Activation energy of both the internal oxidation and the γ′ particle free zones for the present study of RR1000.

Figure 1

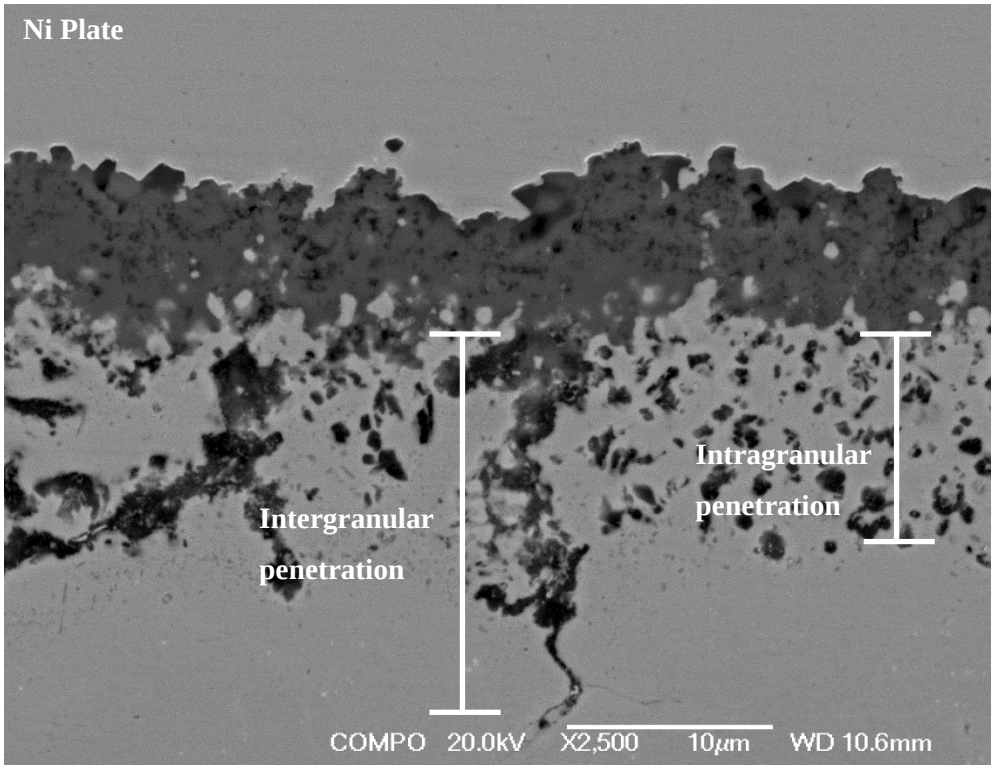
Ni Plate
Intergranular penetration
Intragranular penetration
COMPO 20.0kV X2,500 10μm WD 10.6mm

Figure 2

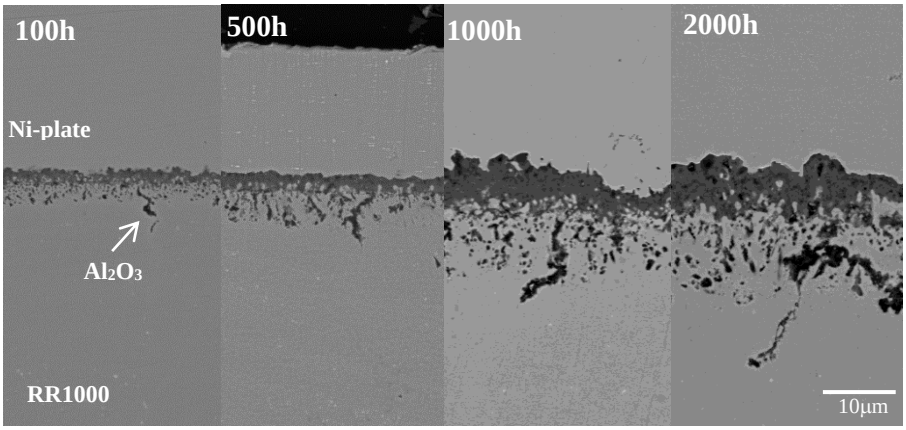

Figure 3

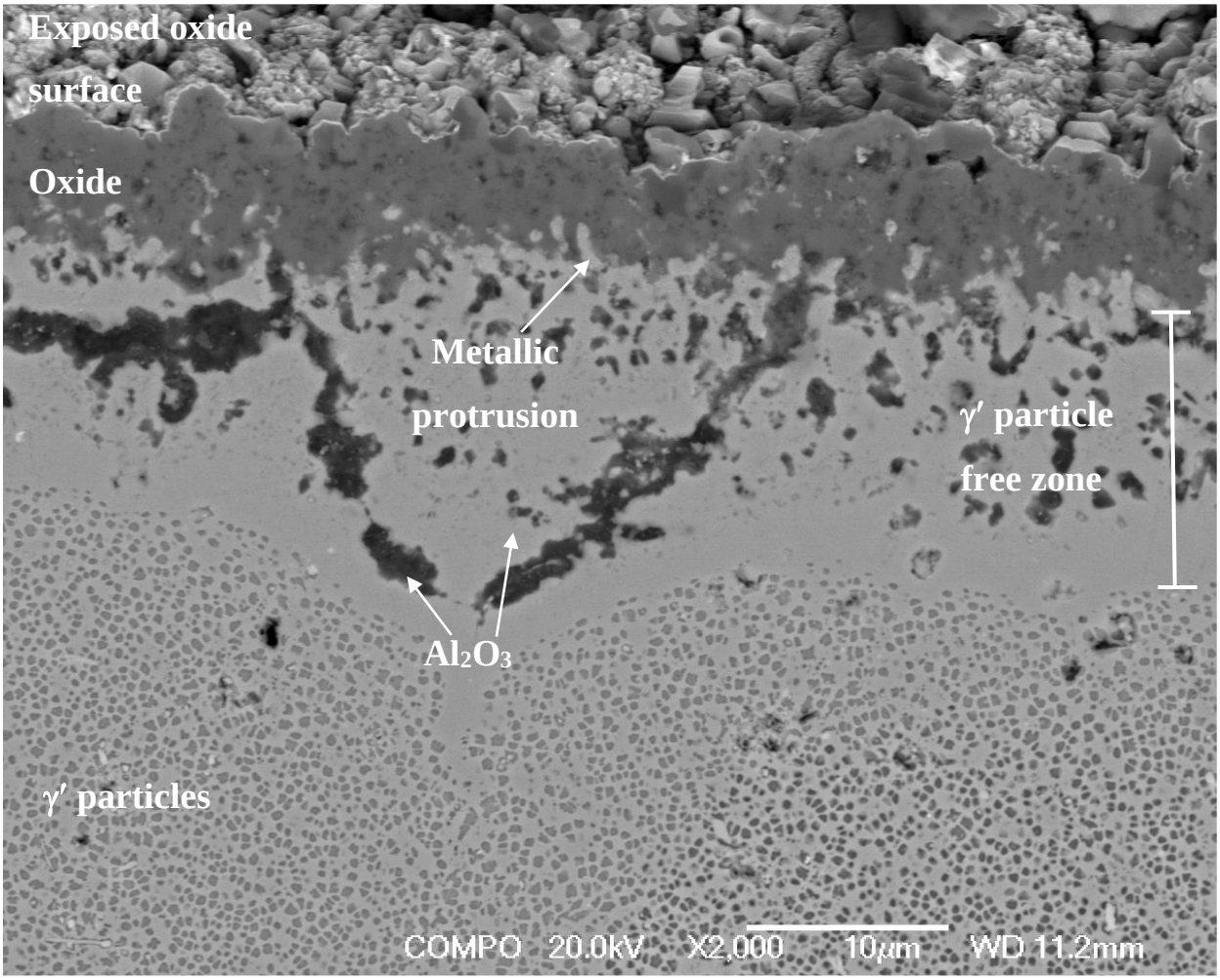
Exposed oxide surface
Oxide
Metallic protrusion
γ′ particle free zone
Al_2O_3
γ′ particles
COMPO 20.0kV X2,000 10μm WD 11.2mm

Figure 4

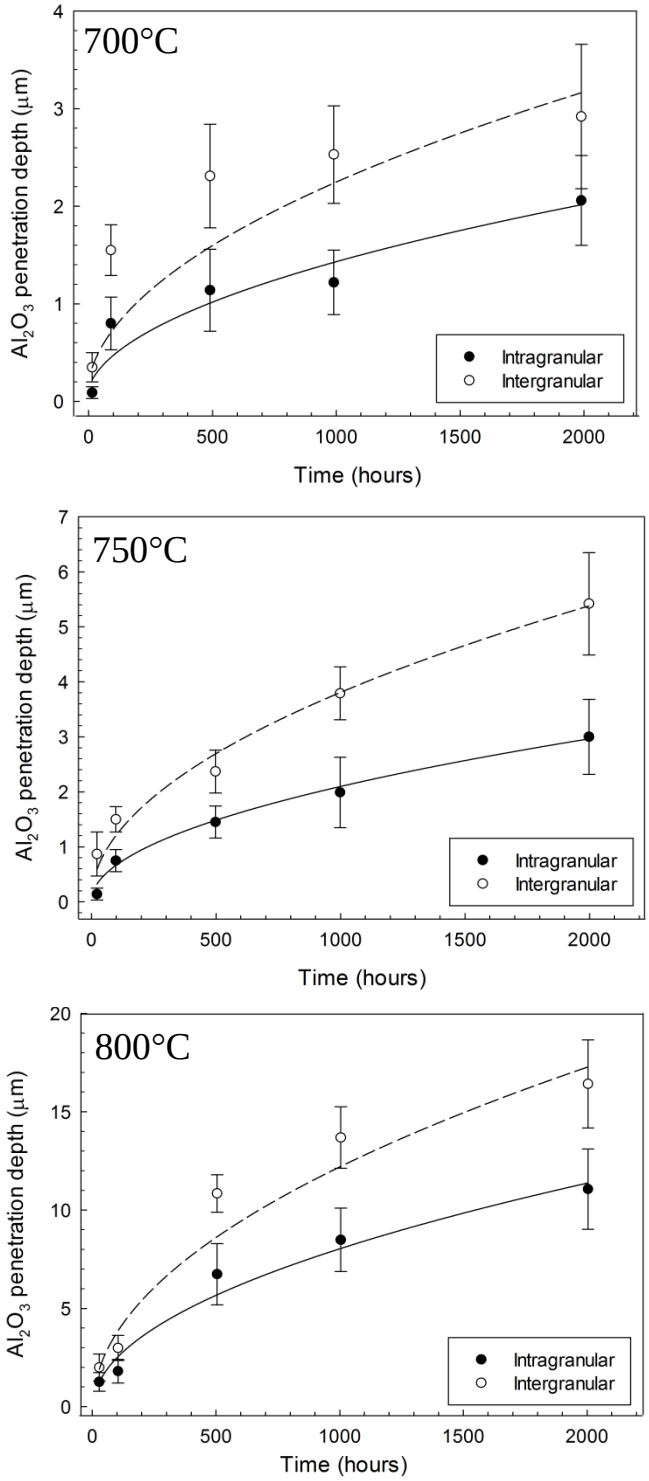
700°C
750°C
800°C
Al_2O_3 penetration depth (μm)
Time (hours)
Intragranular
Intergranular
0
500
1000
1500
2000

Figure 5

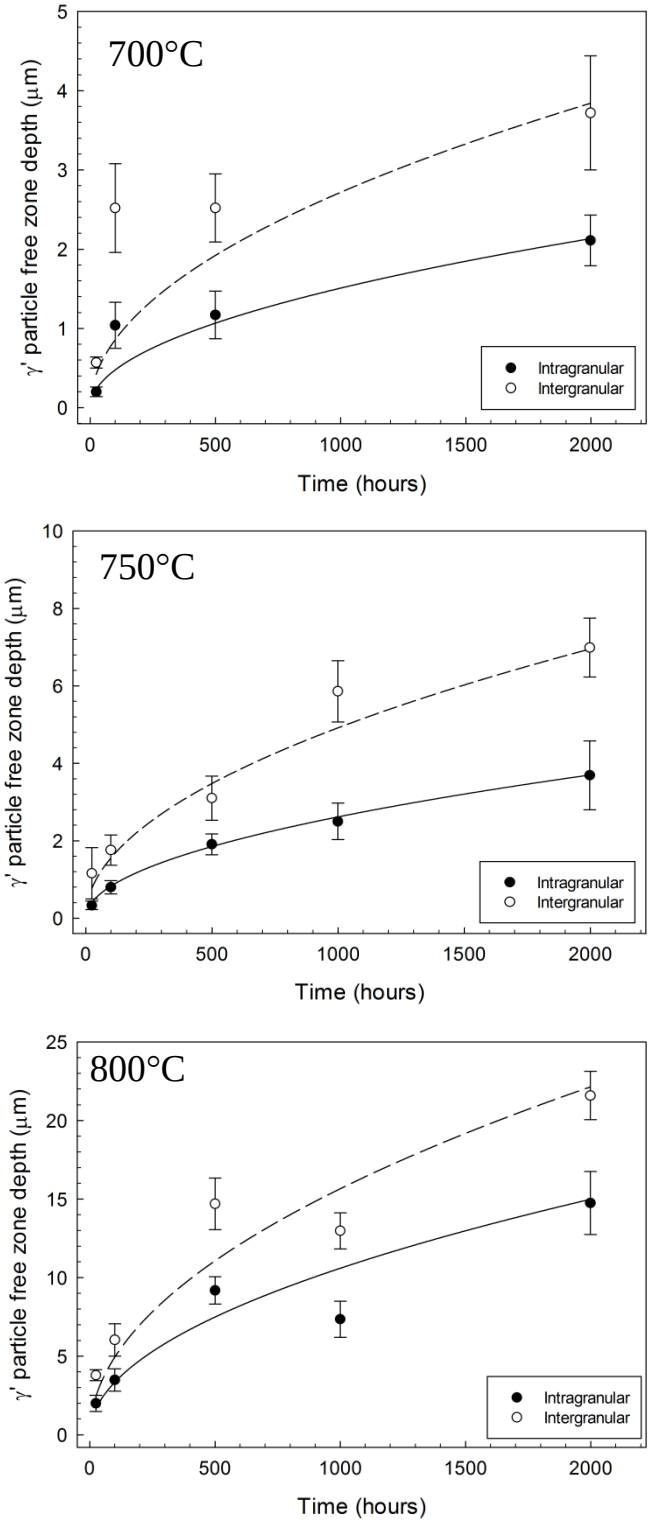
700°C
750°C
800°C
γ' particle free zone depth (μm)
Time (hours)
Intragranular
Intergranular

Figure 6

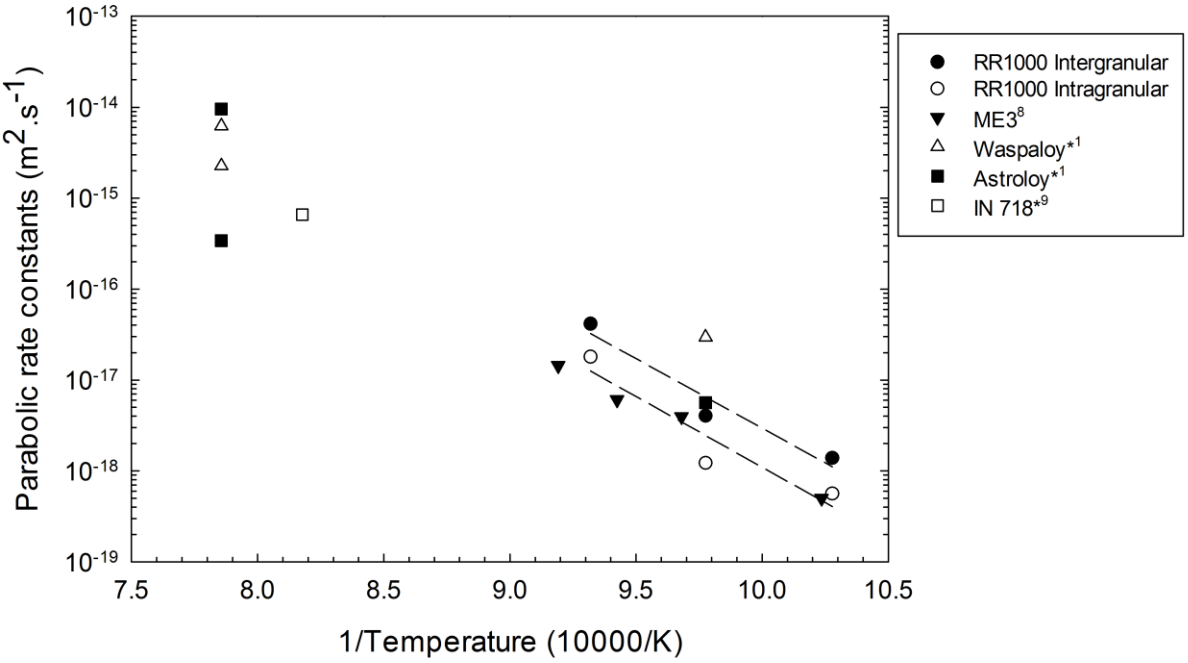
Parabolic rate constants (m2.s-1)
10-13
10-14
10-15
10-16
10-17
10-18
10-19
7.5
8.0
8.5
9.0
9.5
10.0
10.5
1/Temperature (10000/K)
RR1000 Intergranular
RR1000 Intragranular
ME3[8]
Waspaloy*[1]
Astroloy*[1]
IN 718*[9]

Figure 7

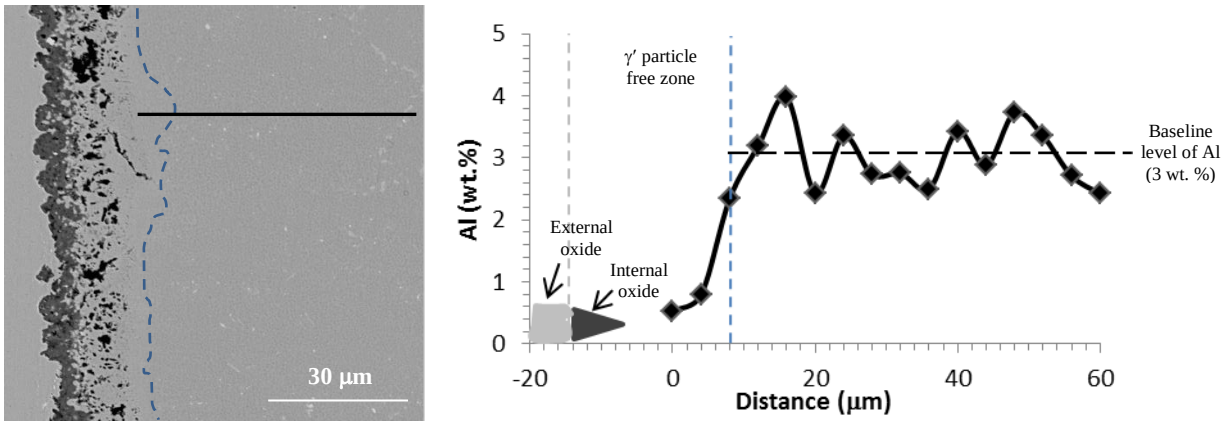
30 µm
γ′ particle
free zone
External
oxide
Internal
oxide
Baseline
level of Al
(3 wt. %)
Al (wt.%)
Distance (µm)
0
1
2
3
4
5
-20
0
20
40
60

Table 1

	Ni	**Co**	**Cr**	**Mo**	**Ti**	**Al**	**Ta**	**Hf**	**Zr**	**C**	**B**
Weight %	Bal	18.5	15.0	5.0	3.6	3.0	2.0	0.5	0.06	0.02	0.03
Atomic %	Bal	17.9	16.5	3.0	4.3	6.35	0.63	0.16	0.04	0.14	0.10

Table 2

Units / μm	**Average Al_2O_3 penetrations**		**Average γ′ particle free zone**	
	Intragranular	**Intergranular**	**Intragranular**	**Intergranular**
Number of measurements	50	10	50	10
Distribution of values	Normal	Normal	Normal	Normal
700°C for 2000h	2.06 (± 0.46)	2.92 (± 0.48)	2.11 (± 0.32)	3.72 (± 0.72)
750°C for 2000h	3.00 (± 0.68)	5.42 (± 0.93)	3.69 (± 0.89)	6.99 (± 0.79)
800°C for 2000h	11.07 (± 2.04)	16.42 (± 2.24)	14.75 (± 2.00)	21.59 (± 1.54)

Table 3

Units / $m^2.s^{-1}$	**Al_2O_3 penetrations**		**γ' particle free zone**	
	Intragranular	**Intergranular**	**Intragranular**	**Intergranular**
700°C	$5.6x10^{-19}$	$1.4x10^{-18}$	$6.3x10^{-19}$	$2.1x10^{-18}$
750°C	$1.2x10^{-18}$	$4.0x10^{-18}$	$1.9x10^{-18}$	$6.7x10^{-18}$
800°C	$1.8x10^{-17}$	$4.2x10^{-17}$	$3.1x10^{-17}$	$6.8x10^{-17}$

Table 4

Al_2O_3 penetrations		**γ′ particle free zone**	
Intragranular	**Intergranular**	**Intragranular**	**Intergranular**
297 $kJ.mol^{-1}$	293 $kJ.mol^{-1}$	336 $kJ.mol^{-1}$	302 $kJ.mol^{-1}$